ORIGINAL PAPER

The role of sediment composition and behavior under dynamic loading conditions on slope failure initiation: a study of a subaqueous landslide in earthquake-prone South-Central Chile

Gauvain Wiemer · Jasper Moernaut · Nina Stark · Philipp Kempf · Marc De Batist · Mario Pino · Roberto Urrutia · Bruno Ladrón de Guevara · Michael Strasser · Achim Kopf

Abstract Subaqueous slope failure mechanisms are still poorly understood partly because they are difficult to study due to the remote location of submarine landslides. Landslides in lakes are smaller in size and more readily accessible and therefore represent a good alternative to their marine counterparts. Lake Villarrica, located in South-Central Chile, experienced significant slope failure and serves here as an exemplary study area for subaqueous landslide initiation mechanisms in tectonically active settings. Coring and CPTU testing were undertaken with the MARUM free-fall CPTU deployed adjacent to the coring sites where all lithological units involved in the slope failure were sampled. Using geotechnical methods such as pseudo-static factor of safety analysis and cyclic triaxial testing, three types of soils (i.e., diatomaceous ooze, volcanic ash, and quick clay) were analyzed for their role in slope failure, and earthquake shaking was identified as the primary trigger mechanism. The investigated landslide consisted of two distinct phases. During the first phase, slope failure was initiated above a tephra layer. In the second phase, retrogression led to the shoreward extension of the slide scarp along a second failure plane located in a stratigraphically deeper, extremely sensitive lithology (i.e., quick clay). Results show that liquefaction of buried tephra layers was unlikely, but such layers might still have contributed to a reduction in shear strength along the contact area with the neighboring sediment. Furthermore, cyclic shaking-induced pore pressure in diatomaceous ooze may be similar to that in granular soils. We generally infer that failure mechanisms observed in this study are equally important for landslide initiation in submarine settings as diatomaceous ooze intercalated with volcanic ash may be abundantly present along active continental margins.

Keywords Landslide · Earthquake shaking · Tephra · Quick clay · Diatomaceous ooze · CPT · Cyclic loading

G. Wiemer (✉) · A. Kopf
MARUM, Centre for Marine Environmental Sciences, Bremen, Germany
e-mail: gwiemer@marum.de

J. Moernaut · M. Strasser
Geological Institute, ETH Zürich, Zurich, Switzerland

J. Moernaut · P. Kempf · M. De Batist
Renard Centre of Marine Geology, Ghent University, Ghent, Belgium

J. Moernaut · M. Pino
Facultad de Ciencias, Universidad Austral de Chile, Valdivia, Chile

N. Stark
Department of Civil and Environmental Engineering, Virginia Tech, Blacksburg, VA, USA

R. Urrutia
Centro EULA, Universidad de Concepción, Concepción, Chile

B. L. de Guevara
BENTOS, Santiago, Chile

Introduction

Submerged slope sediments located in seismically active settings may experience failures which may entail devastating and dramatic aftermaths for onshore and offshore infrastructure as well as coastal communities (Hampton et al. 1996). For the purpose of slope stability risk assessment and landslide-caused damage mitigation, it is of primary importance to thoroughly understand the initiation mechanisms of a variety of previous subaqueous slope failure
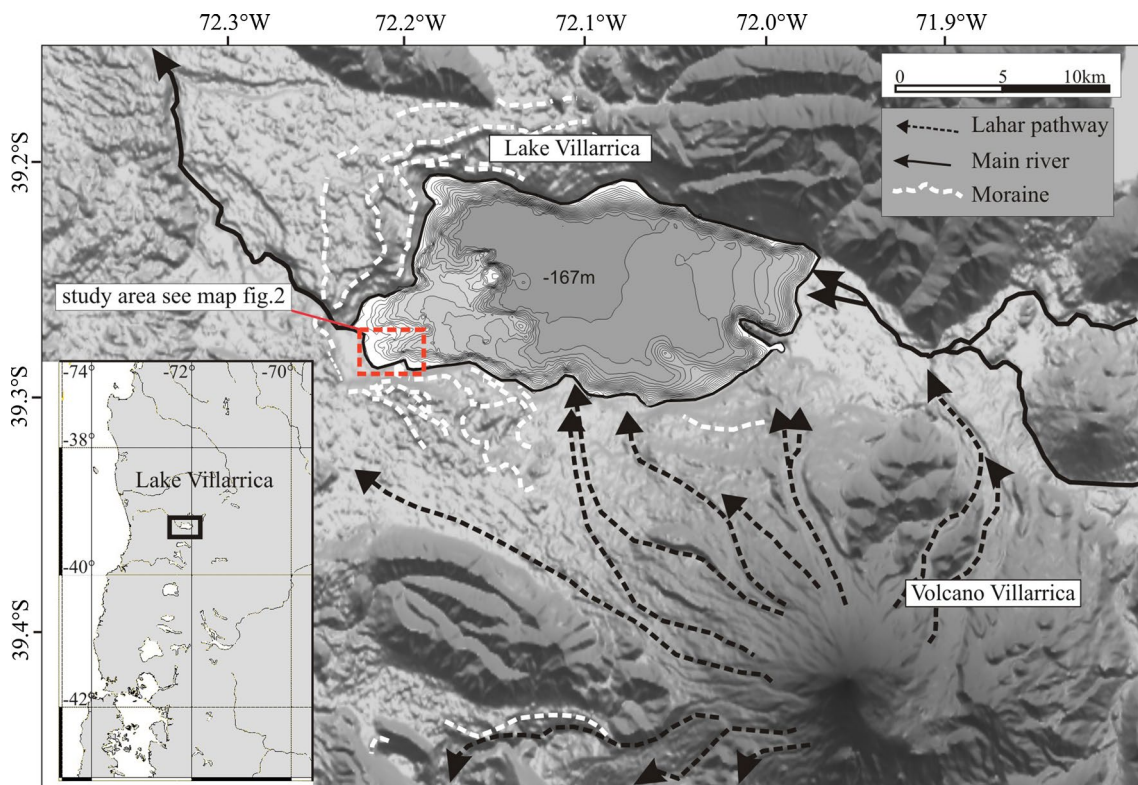
events and their inherent complexity (Leroueil et al. 1996). A detailed analysis of the failure plane and investigation of the failure mechanism often turn out to be an expensive and challenging undertaking in the marine realm. Drilling is usually the only possibility to reach crucial lithologies at depth. Drilling platforms are not available in many projects; hence, data from surface lithologies are extrapolated based on assumptions and approximations that could lead to uncertainties and biases in the assessment of "in situ" conditions and the failure plane. Additionally, sediment along active margins often also contains layers of diatomaceous ooze and volcanic ash whose geotechnical properties are still poorly understood. Volcanic ashes, for instance, have been proposed to represent preferential failure planes or weak layers in earthquake-prone submarine settings due to their high liquefaction potential (Sassa et al. 2012; Harders et al. 2010). However, investigations of their mechanical strength are rare. Diatomaceous ooze has low bulk density and high moisture content because of the hollow structure of the diatom frustules which contain water. Index properties may be biased due to the trapped water. Diatoms can provide delayed compressibility or a sudden increase in compressibility once the yield strength of the microfossil

is exceeded (Volpi et al. 2003). The frictional behavior of diatomaceous oozes is majorly influenced by the size and shape of their constituents (Locat and Tanaka 2001).

Unlike in the marine realm, access to failure planes in lakes is often easier and more cost-effective (Strasser et al. 2007; Stegmann et al. 2007). Furthermore, slope failure in lakes may have devastating consequences similar to marine slides (Kremer et al. 2012).

Lake Villarrica (Fig. 1) is located in South-Central Chile. A previous seismic-stratigraphic analysis performed in the southwestern region of the lake revealed voluminous mass-wasting deposits and indicated the presence of vertical subsurface fluid flow in the region (Moernaut et al. 2009). Large earthquakes occur regularly in South-Central Chile and are one of the most cited short-term triggering mechanisms for landslide initiation (Sultan et al. 2004). Earthquake shaking has been suggested as the most probable cause for slope failure in Lake Villarrica (Moernaut et al. 2009).

This study represents a reassessment of the previous hypothesis by investigating geotechnical properties of Lake Villarrica's sedimentary succession, including its failure planes at high spatial resolution. The study focuses on a

Fig. 1 Morphological setting of Lake Villarrica modified after Moernaut et al. (2009). Lake-surrounding topography is derived from SRTM data. Sun illumination is from the North. Moraine locations ("Llanquihue" moraine belt) are based on Laugenie (1982). Lahar pathways are derived from Laugenie (1982) and satellite imagery. Lake Villarrica: Bathymetric contours are shown every 10 m. The deepest part is 167 m below lake level (based on SHOA 1987)

confined area with a landslide in the SW region of the lake that is clearly visible in the bathymetry. We present a broad set of field and laboratory geotechnical data, including the results of an earthquake simulation derived during cyclic triaxial tests. The pseudo-static factor of safety is calculated based on a continuous data set of "in situ" undrained shear strength. In combination with the spatial information derived from seismic reflection and multi-beam data, this data set allows us to carry out a detailed analysis of a subaqueous landslide and explain the location of the slope failure initiation.

Setting

Lake Villarrica is a large glacigenic lake (ca. 20 km × 10 km) located at the foot of Villarrica Volcano in the Andes, in South-Central Chile. The lake basin originated from glacial valley overdeepening, and the formation of large frontal moraine ridges during the Late Quaternary glaciations (Laugenie 1982). The landscape around the lake is dominated by Villarrica Volcano, one of South America's most active volcanoes (Witter et al. 2004).

Tectonically, our study area is controlled by the slightly oblique subduction of the Nazca Plate under the South American Plate, which occurs at a present convergence rate of about 6.6 cm/year and an azimuth of about N78°E (Angermann et al. 1999). Large megathrust earthquakes, such as the giant AD 1960 Valdivia earthquake (Mw: 9.5) or the 2010 Maule earthquake (Mw: 8.8), result from this subduction and have a strong impact on the landscape of South-Central Chile (Moernaut et al. 2014). The Valdivia earthquake, for instance, reached Modified Mercalli Intensity of VII to XI in the Chilean Lake District (Duke and Leeds 1963) and triggered numerous subaerial and subaqueous landslides (Chapron et al. 2006; Moernaut et al. 2007). The reoccurrence interval of earthquake with an intensity comparable to the one AD 1960 is in the range of a century to multi-century in our study area as shown by historical and paleoseismological evidence (Cisternas et al. 2005; Moernaut et al. 2007; Blumberg et al. 2008; Lomnitz 2004).

Bathymetry and subsurface imaging

In 2013, high-resolution bathymetry data were acquired using an R2Sonic 2024 multibeam system (200–400 kHz) deployed on R/V Bentos Surveyor of the survey company BENTOS (Santiago, Chile). Vessel position was determined using real-time kinematic (RTK)-corrected GPS with a horizontal accuracy of ~0.1 m (OmniSTAR G2). Multi-beam swath angle and frequency were modified online depending on the water depth and data quality. Data processing and visualization were carried out using the Comprehensive Hydrographic and Sonar Data Processing System (CARIS HIPS and SIPS) and Geographic Information System (GIS) software.
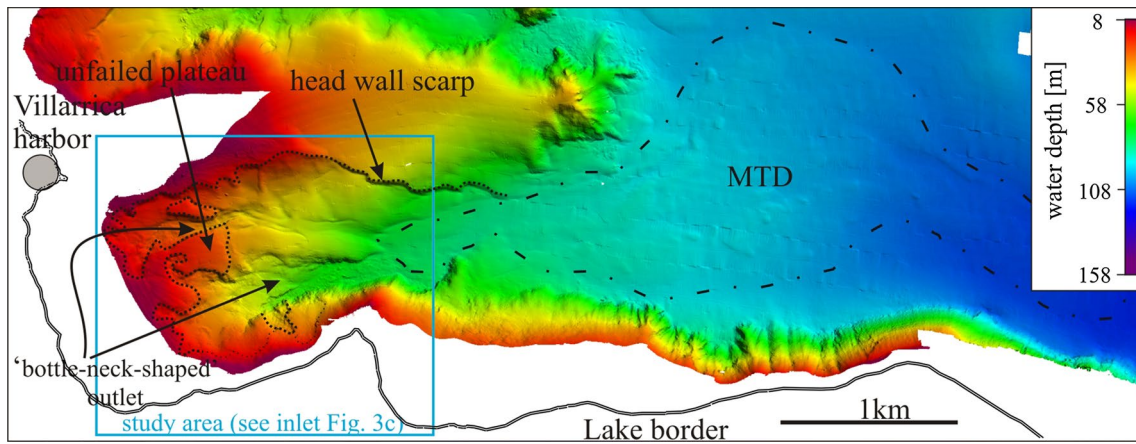
Additional to the data collected in 2001 and 2007 (Moernaut et al. 2009), single-channel high-resolution (pinger, 3.5 kHz) seismic data were acquired in 2011 to improve spatial resolution of the slide area. Navigation and positioning were carried out using stand-alone GPS (horizontal accuracy of ±5 m) on the Huala II, a small research vessel from the Universidad Austral de Chile. At a shotpoint spacing of about 1–1.5 m, the acoustic signal of the pinger penetrated the sedimentary fill by up to ~20 m (i.e., 25–30 ms TWT) with a vertical resolution of 15–20 cm. Data were recorded digitally on a TRITON-ELICS Delph-2 acquisition system. Seismic-stratigraphic interpretation was done using Seismic Micro-Technology (SMT) Kingdom Suite after applying a frequency band-pass filter. Water and subsurface depths were calculated using a mean acoustic velocity of 1.500 m/s.
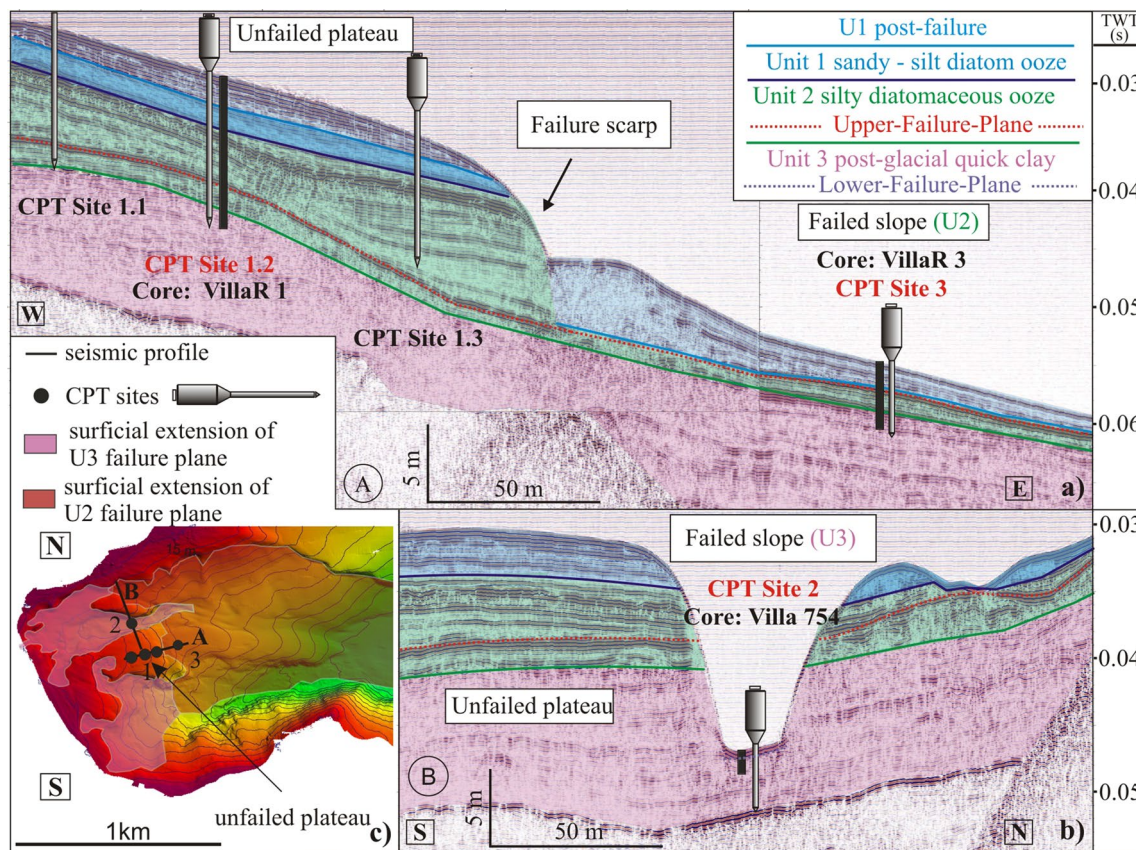
Slide geometry and sedimentology

The multi-beam bathymetry map of the slide area is presented in Fig. 2. The slide affected an area of about 0.8×10^6 m^2 and mobilized a volume of ~6×10^6 m^3 of sediment. The run-out distance of the slide is about 5.4 km. The head wall height is ~7–11 m. The average slope angle is 2.7°. The slide is characterized by an irregular head scarp (Fig. 2). The up-slope section of the slide is divided into a northern and southern part by an unfailed plateau which is located at the centre of the excavated area.

Two perpendicular seismic profiles (A and B) are presented in Fig. 3a, b. The profiles represent cross sections that run in approximately the E–W (A) and N–S direction (B) and are showing parts of the unfailed plateau, the failure scar, and a portion of the failed slope. The unfailed plateau as seen in Fig. 3a, b comprises the entire "uppermost seismic unit" as identified by Moernaut et al. (2009). This seismic unit is uniformly draped on top of an irregular basement morphology. The uppermost seismic unit spans 17.5–17.15 ka BP to present (McCulloch et al. 2000).

From top to bottom, three seismic subunits (U1–U3) are distinguished on both profiles. Unit 1 (U1) is characterized by continuous reflections running parallel to the slope. U1 represents plateau sediment and reveals little change in thickness. Unit 2 (U2) equally shows continuous, but subparallel reflectors with spatial differences in the down-slope direction. Both units (U1 and U2) build a drape with low-to-high reflection strength, hence alternating low-to-high

Fig. 2 Multi-beam bathymetric map for the SW part of Lake Villarrica (location: see Fig. 1) with indication of the geotechnical study area (*blue frame*). MTD: Mass transport deposit described in detail in (Moernaut et al. 2009)

Fig. 3 **a** E–W orientated, seismic profile A including CPT sites 1.1, 1.2, 1.3, and 3, and coring location of VillaR 1. CPT sketch illustrates CPT position and penetration depth. *Thick vertical black line* indicates coring locations and depth. *Light blue zone*: post-failure Unit 1. *Dark blue*: pre-failure Unit 1. *Green zone*: Unit 2. *Dusky pink zone*: Unit 3. *Red dotted line*: upper failure plane. **b** Seismic profile B including CPT site 2 and coring location of Villa 754. **c** Bathymetric map of the SW part of Lake Villarrica including location of seismic profile A and B and CPT positions. Isobaths every 5 m. *Reddish area*: extent of the "upper failure plane" that developed within silty diatomaceous ooze (Unit 2), immediately overlying a tephra (SFPT). *Dusky pink area*: extent of the quick clay (U3) sliding surface

impedance. Unit 3 (U3) is characterized by a seismic facies that is chaotic and has a lower amplitude than U1 and U2.

Judging from the seismic images, it seems that the stratigraphic horizon corresponding to the failure plane is much deeper in profile B (i.e., within U3) compared to profile A (i.e., within U2). This fact indicates that the landslide event took place at two distinct stratigraphic levels (U2 and U3) (Fig. 3a, b). The spatial extents of these stratigraphic levels are mapped in Fig. 3c. The upper part of the slide scar (i.e., the area surrounding the unfailed plateau) is characterized by an irregular head scarp and a "bottle-neck-shaped" outlet. The lower head scarp area, where the upper stratigraphic level acted as a failure plane, is more regular and confined.

In the following, these two failure horizons will be termed "lower failure plane" (in U3) (see profile B Fig. 3b) and "upper failure plane" (in U2) (see profile A Fig. 3a). However, the location of failure initiation cannot be inferred from seismic data alone. Competing interpretations are (1) retrogressive failure or (2) that failure initiated up-slope at a deeper stratigraphic level and stratigraphically stepped-up to a shallower level when progressing down slope [stratigraphic "step-up" see (Moernaut and De Batist 2011)].

Field data acquisitions

Coring

In order to study slope failure from a sedimentological point of view, multiple hammer-driven piston cores (VillaR 1–5) and gravity cores (Villa 754-1 to 754-4) were taken from the unfailed plateau (site 1 Fig. 3a, c) and within the slide scar (site 2 and 3 Fig. 3a–c). Sediment cores had a diameter of 60 mm and a maximum length of ~8 m with a maximum core-section length of 3 m. At each coring site, a second core was taken adjacent to the first core with a vertical offset of 1 m in order to cover potential gaps between two sections of the first core. A detailed description of the coring tool can be found in Bertrand (2005).

Coring site VillaR 1 serves as reference site and is located at the centre of the unfailed plateau (Fig. 3c). This core (VillaR 1) provides intact samples from the upper and lower stratigraphic levels that acted as failure planes on the slope. The core VillaR 3 (site 3 Fig. 3a) and the gravity cores (site 2 Fig. 3b) were taken within the failure scars.

Cone penetration testing

The MARUM cone penetration testing device (CPT) (Stegmann et al. 2006) was deployed to obtain the "in situ" geotechnical properties of the unfailed and disturbed stratigraphic units. The locations of three main CPT sites adjacent to the coring positions were selected based on the results of the seismic investigation. A total of 28 measurements were conducted on the unfailed plateau and within the slide area (see Fig. 3 for exact positioning). Cone resistance (q_c), sleeve friction (f_s), and pore pressure (u) were measured down to a maximum depth of ~8.1 m.

The "in situ" undrained shear strength (s_u) is a function of the strain rate (Dayal and Allen 1975) and pore pressure-corrected cone resistance ($q_{t,qs}$) (i.e., the quasi-static cone resistance), the total overburden stress (σ_{v0}) and an empirically determined cone penetration resistance factor ($N_{k,t}$) which is related to q_t [for details, see (Lunne et al. 1997)]. s_u was determined using:

$$s_u = \frac{q_{t,qs} - \sigma_{v0}}{N_{kt}} \qquad (1)$$

s_u was derived using a standard cone factor (N_{kt}) of 12–16 for normally and overconsolidated clays, respectively. The total overburden stress (σ_{v0}) was calculated as follows:

$$\sigma_{v0} = \gamma * z \qquad (2)$$

where γ is the unit weight of the sediment and z is the sub-bottom depth. γ was taken as 13.9 kN/m³ based on a mean of bulk density measurements (see Sect. 7.1) obtained with a Multi-Sensor Core Logger (MSCL).

The state of consolidation derived from CPT

The state of consolidation was estimated by examining the "normalized shear strength," i.e., the ratio of undrained shear strength and effective overburden stress (s_u/σ'_{v0}). The effective overburden stress was calculated assuming hydrostatic pore pressure at depth:

$$\sigma'_{v0} = \gamma' * z \qquad (3)$$

where γ' is the submerged unit weight of the sediment.

Note that the assumption of hydrostatic pore pressure leads to a minimum value of normalized undrained shear strength (s_u/σ'_{v0}) because we assume the maximum effective overburden stress. Therefore, the values obtained from this calculation are conservative.

The normalized undrained shear strength of normally consolidated organic and inorganic soils is considered to be in the range of 0.2–0.3 (Karlsson and Viberg 1967). However, fossiliferous soils may be characterized by a normalized undrained shear strength of up to ~0.4 at normal consolidation (Tanaka et al. 2012). Thus, any soil with $s_u > 0.4 * \sigma'_{v0}$ is considered as overconsolidated and any soil rich in diatom frustules (>70 %) with $s_u < 0.3 * \sigma'_{v0}$ may be considered as underconsolidated from a geotechnical perspective.

Pseudo-static factor of safety analysis

s_u was further used as input parameter in a one-dimensional, undrained, infinite slope stability analysis (Morgenstern and Price 1965). The pseudo-static factor of safety (FS) is the ratio of resisting forces to driving forces acting on slope sediment during earthquake shaking whereby earthquake-induced shear stresses are considered to be constant over the period of shaking (Hampton et al. 1996). If FS > 1, slope sediment may be considered as stable, whereas FS < 1 indicates failure under tested conditions (Morgenstern and Price 1965). FS is defined as:

$$FS = \frac{s_u}{\sigma'_{v0}\left(\sin(\alpha)\cos(\alpha) + k\left(\frac{\gamma}{\gamma'}\right)\cos^2(\alpha)\right)} \tag{4}$$

where γ is the bulk unit weight, k is the seismic coefficient, and α is the slope angle. Again, the values obtained from this equation are to be considered as conservative as they correspond to minimum values due to the assumption of hydrostatic pressure at depth.

The FS is critically dependent on the seismic coefficient (k) which describes the additional shear stress induced by the propagation of seismic shear waves. In theory, the value of the seismic coefficient should depend on some measure of the amplitude of the inertial force induced in the slope by the dynamic forces generated during an earthquake. Because soil slopes are not rigid and the peak acceleration generated during an earthquake lasts for only a very short period of time, seismic coefficients used in practice generally correspond to acceleration values well below the predicted peak accelerations (Kramer 1996). In order to select an appropriate k value, past earthquake peak ground acceleration (PGA) was linked to k values using the following relation proposed by Hynes-Griffin and Franklin (1984):

$$k = 0.5\frac{PGA}{g} \tag{5}$$

In Villarrica, the Modified Mercalli Intensity (MM) of the earthquake with the largest ever recorded magnitude, the 1960 Great Chilean Earthquake, corresponded to VII 1/2 (very strong) (Lazo Hinrichs 2008). The 2010 Chile earthquake led to an intensity of VI 3/4 (MM) (USGS 2010). Shaking intensity values of VI to VIII can be induced by earthquakes with a peak ground acceleration (PGA) of 2.5–20 % g, respectively (Medvedev 1977). The FS was calculated for k values of 0.0125, 0.0375, 0.1, and $\alpha = 3°$, 5°, and 7° in order to explore the influence of slope angle and earthquake magnitude variation. The actual slope angle at the head scarp is 5° as inferred from reflection seismic profiles. The bulk density was set to 1.4 g/cc according to MSCL data (see Sect. 7.1). The k values we chose for the FS analysis represent a range of scenarios (PGA of 2.5, 7.5,

and 20 % g) that may reoccur in the near future. However, the k value does not account for earthquake-induced excess pore pressure build up and inherent sediment shear strength reduction. These elements can be simulated in laboratory cyclic triaxial shear experiments (see Sect. 6.3.2).
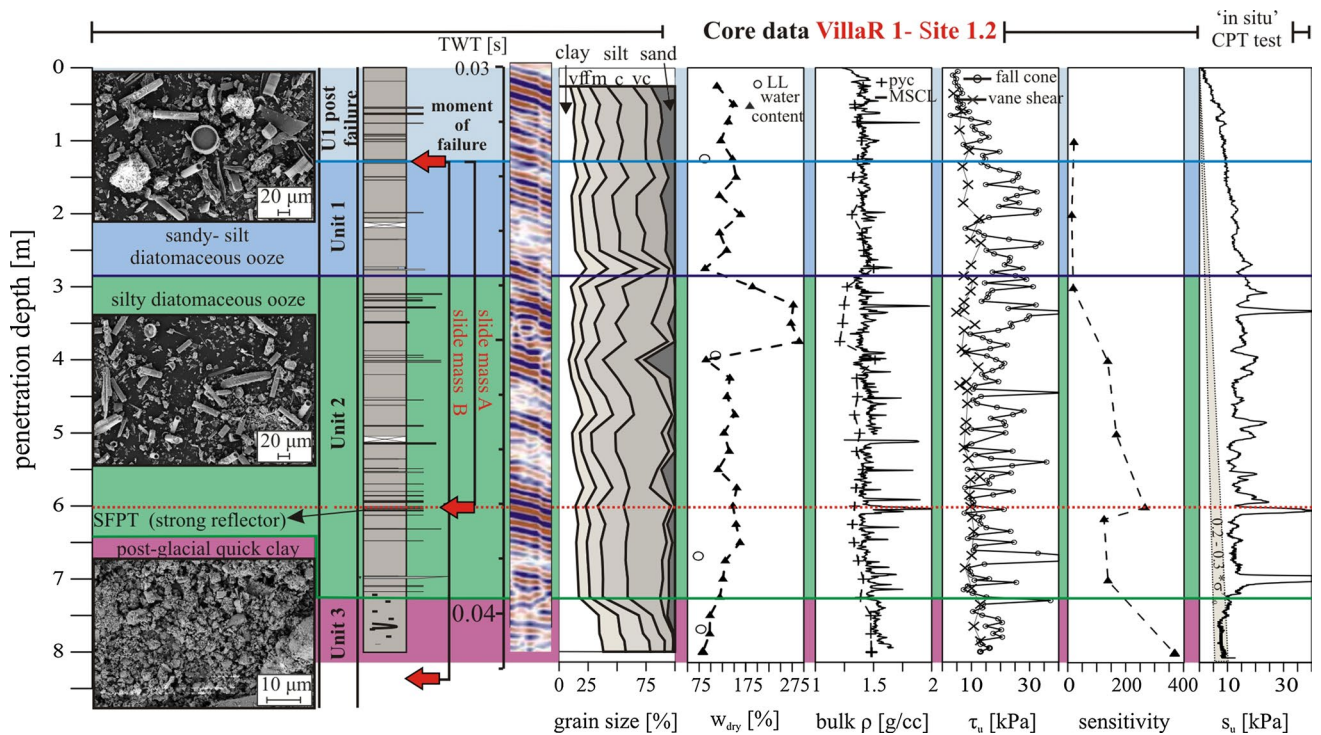
Laboratory data acquisition

Index properties

Magnetic susceptibility, gamma ray attenuation bulk density, and compressional wave velocity were measured on whole cores (i.e., whole round or WR) using the GEOTEK Multi-Sensor Core Logger (MSCL), at the Limnogeology Laboratory, ETH Zürich. All cores were then transported to the geotechnical laboratories at MARUM (Centre for Marine Environmental Sciences, Bremen) where they were split, photographed, and sedimentologically described. Further analysis included the measurement of the sediment's natural water content (w_n %) at 25 cm intervals immediately after splitting. Samples were oven-dried for at least 24 h at 60 °C, and solid volume was determined using a helium pycnometer to derive grain density, bulk density, and void ratio. Grain size distributions were measured via laser diffraction analysis with a Coulter LS-13320 that quantifies grain size contents in 117 classes ranging from 0.04 to 2,000 µm as a volume percent (vol.%) (see Syvitski et al. 1991; Loizeau et al. 1994 for details). Laboratory-based measurement of undrained shear strength (τ_u) were taken on the split cores using (1) a Wykeham-Farrance cone penetrometer WF 21600 according to British Standards Institutions (BS 1377) (British-Standard-Institute 1977; Hansbo 1957) and (2) a motorized Wykeham-Farrance vane shear apparatus (rotation rate = 90°/min) (Blum 1997) with a spacing of ~5 and ~25 cm, respectively. Remolded shear strength at w_n % of selected samples was measured using a Haake RV-20 Vane Shear Rotovisco apparatus (rotation rate = 90°/min) in order to derive sensitivity, which is defined as the ratio of undrained shear strength (τ_u) over remolded undrained shear strength (τ_{ru}) (Chaney and Richardson 1988). Atterberg limits were determined with a Casagrande apparatus according to ASTM Standard D4318-05 (ASTM 2000). Scanning electron microscopy (SEM) was performed on samples representative for the different lithologic units of VillaR 1 (Fig. 4).

One-dimensional consolidation tests

One sample out of each seismic unit was tested in one-dimensional consolidation experiments (i.e., oedometer tests) following the DIN 18135 (Deutsches Institut für Normung 2012) in order to obtain further insight in the state of consolidation and hydraulic conductivity of the sediment.

Fig. 4 Index properties of the sediment core VillaR 1 (site 1) including (from *left* to *right*): **a** SEM image of each unit, a litholog after visual core description, an indication of the slide sediment portions A and B, a short segment of seismic reflection data, results of: grain size analysis, natural water content (w_n), bulk density (ρ), laboratory-based measurements of undrained shear strength (τ_u), sensitivity, and "in situ" undrained shear strength (s_u). Shear strength data are clipped at 40 kPa. Horizontal lines separate the different units whereby U1 is divided in a pre- and post-failure deposit. *Dashed horizontal red line*: location of the "upper failure plane" right above the SFPT

Cylindrical samples of 56 mm in diameter and 14.8 mm height (H) were placed in an oedometer cell and compressed in uniaxial direction under drained conditions and full horizontal constrainment. The state of consolidation or overconsolidation ratio is determined using the ratio of maximum pre-consolidation stress ($\sigma'_{v,m}$) to the calculated present effective overburden stress ($\sigma'_{v,0}$) (OCR $= \sigma'_{v0}/\sigma'_{v0,m}$). The pre-consolidation stress ($\sigma'_{v,m}$) was determined following the rebound method proposed by Schmertmann (1953).

Samples of U1 and U2 were taken at site 1 at a depth of 1.98 and 6.4 mblb (meter below lake bottom), respectively. U3 was sampled at site 3 at a depth of 3.69 mblb. At the moment of failure, the sample of U3 must have been buried under at least 8.5 m of U1 and U2 sediment (deduced from reflection seismic data) and additional 0.5 m of U3 sediment. Therefore, to calculate the overconsolidation ratio (OCR $= \sigma'_{v0}/\sigma'_{v0,m}$) for the U3 sample, we assume a past minimum sediment drape of 9 m.

Vertical hydraulic conductivity (k_f) of each sample was determined following the DIN 18135 (Deutsches Institut für Normung 2012):

$$k_f = c_v * m_v * \gamma_w \tag{6}$$

where c_v is the coefficient of consolidation:

$$c_v = 0.848(H_0/2)^2/t_{90} \tag{7}$$

m_v is the coefficient of volume compressibility:

$$m_v = 1/H_0 * (H_0 - H_1/\sigma'_1 - \sigma'_0) \tag{8}$$

γ_w is the unit weight of water. t_{90} is the time required for 90 % completion of primary consolidation derived according to Schmertmann (1953). H_0 and H_1 are the sample height at the beginning and end of each consolidation step. σ'_0 and σ'_1 are the effective vertical stresses of two subsequent loading steps.

Advanced geotechnical laboratory shear experiments

Key lithologic units were tested for their drained static and undrained cyclic shear strength in order to characterize the sediment's behavior under static gravitational and earthquake loading conditions, respectively. One particular tephra layer was simulated by sieving tephra that was sampled on the Villarrica Volcano flank to equivalent grain size distribution. By doing so, we obtained sufficient material to determine the minimum and maximum density according to DIN-Norm 1826 (Deutsches Institut für Normung 1996).

Table 1 Settings and initial conditions for cyclic triaxial shear experiments

Sample	r_c	q_0 [kPa]	q_c [kPa]	K_0	B value	I_D	H_0 (mm)	N°
U1	1.133	40.268	25	0.500	0.967	n.d	74.643	20
U2	1.193	40.816	25	0.496	0.974	n.d	76.269	10
U3	0.853	20.752	25	0.675	0.950	n.d	73.971	25
SFPT—equival.	1.163	40.048	25	0.502	0.975	0.721	72.057	252
SFPT—equival.	1.173	40.426	25	0.498	0.983	0.551	72.287	136

Shear tests could thus be conducted on lake equivalent tephra material and at approximately equivalent density index. In the following, the original tephra is called "sub-failure plane tephra" (SFPT) (see Sect. 7.1) and the reproduced material "SFPT equivalent."

Direct shear experiments

Drained direct shear tests were performed on cylindrical samples of 56 mm in diameter and ~25 mm height that had been placed in a GIESA RS5 device (see Ikari and Kopf 2011 for details). Tests were performed according to DIN-Norm 18137-3 (Deutsches Institut für Normung 2002). A vertical ram exerts the effective normal stress (σ_n') upon the samples that were sheared under saturated and drained conditions with σ_n' ranging from 50 to 300 kPa. The shear path for each experiment was at least 10 mm. Effective normal stress (σ_n'), shear stress (τ'), and vertical and horizontal displacement were measured at a frequency of 0.1 Hz. Strain rates were set to 0.04 mm/min which is considered sufficiently slow to allow constant drainage and complete pore pressure dissipation. These measurements allowed the calculation of strength parameters according to the Mohr–Coulomb constitutive law:

$$\tau_p' = c' + \sigma_n' * \tan(\varphi) \tag{9}$$

where c' is the effective cohesion, φ, the angle of internal friction, τ_p', the peak shear stress, and σ_n', the effective normal stress, both at failure. In granular materials c' is considered zero (Handin 1969).

Cyclic triaxial undrained shear experiments

Earthquake shaking was simulated via undrained cyclic shear strength experiments using the dynamic triaxial testing device (Kreiter et al. 2010). Seed and Idriss (1971) developed a simplified procedure to convert any arbitrary earthquake signal into uniform loading cycles of equivalent cyclic shear stress amplitude. This method requires using 65 % of the maximum earthquake-induced shear stress (τ_{max}) in the field as uniform cyclic shear stress amplitude in laboratory testing (τ_c):

$$\tau_c = 0.65 \tau_{max} \tag{10}$$

$$\tau_{max} = \frac{PGA}{g} * \sigma_{v,0}' * r_d \tag{11}$$

where r_d is a reduction factor that accounts for the variation of cyclic shear stresses with depth.

Under laboratory conditions, cyclic shear stress is induced by cyclic, vertical loading and unloading of a cylindrical sample at constant lateral stress. The cyclic shear stress is defined as:

$$\tau_c = \frac{q_c}{2} \tag{12}$$

$$q_c = \sigma_{1,max} - \sigma_{1,0} \tag{13}$$

where q_c is the cyclic deviator stress, $\sigma_{1,0}'$ is the initial effective vertical stress, $\sigma_{1,max}'$ is the maximum vertical stress during cyclic loading.

Cylindrical specimens with an area of 10 cm^2 were extracted from WR cores; tephra samples were air-pluviated and tapped to desired densities and assembled in a triaxial cell. Initial effective vertical ($\sigma_{1,0}'$) and lateral ($\sigma_{3,0}'$) stresses were set to 80 and 40 kPa, respectively. All samples were cyclically loaded under initial anisotropic stress conditions, in harmonic, purely compression mode (i.e., $0 < q_{min} < q_c$) with a frequency of 1.0 Hz which is the standard frequency used in earthquake engineering (Kramer 1996). The vertical displacement, cyclic stress, lateral stress, and excess pore pressure evolution (Δu) were recorded during undrained cyclic loading. The pore pressure ratio (PPR) is defined as:

$$PPR = \frac{\Delta u}{p_0} \tag{14}$$

$$p_0 = \frac{(\sigma_{1,0}' + 2 * \sigma_{3,0}')}{3} \tag{15}$$

where p_0 is the initial mean effective normal stress. The number of cycles to failure was determined with failure defined as (1) the onset of liquefaction, defined by a PPR of 0.9 or (2) a gain of 5 % vertical axial strain (ε_v). Details of the testing conditions, including the reversal coefficient (r_c) (Galandarzadeh and Ahmadi 2012), initial deviatoric stress (q_0), cyclic deviatoric stress (q_c), the lateral earth pressure coefficient (K_0), Skempton's B value ($\Delta u / \Delta p_0$) (Skempton

1954), relative density (D_r), initial sample height (H_0), and number of cycles to failure, are given in Table 1. For a more thorough understanding of the influence of each of these parameters, please see (Kramer 1996; Mohamad and Dobry 1986; Youd et al. 2001).

Here, we applied a cyclic shear stress (τ_c) of 12.5 kPa and used $r_d = 0.95$ (~20 m depth) (Seed and Idriss 1971). These cyclic stress parameters correspond to loading at a depth of 20 m during an earthquake with a local PGA of ~25 % g, i.e., a Modified Mercalli Intensity (MM) of VIII (Medvedev 1977). The undrained cyclic shear tests shed light on the dynamic response of the sediment to earthquake shaking, where pore pressure evolution and inherent sediment weakening are primary output information.

Data and results

Sediment characterization
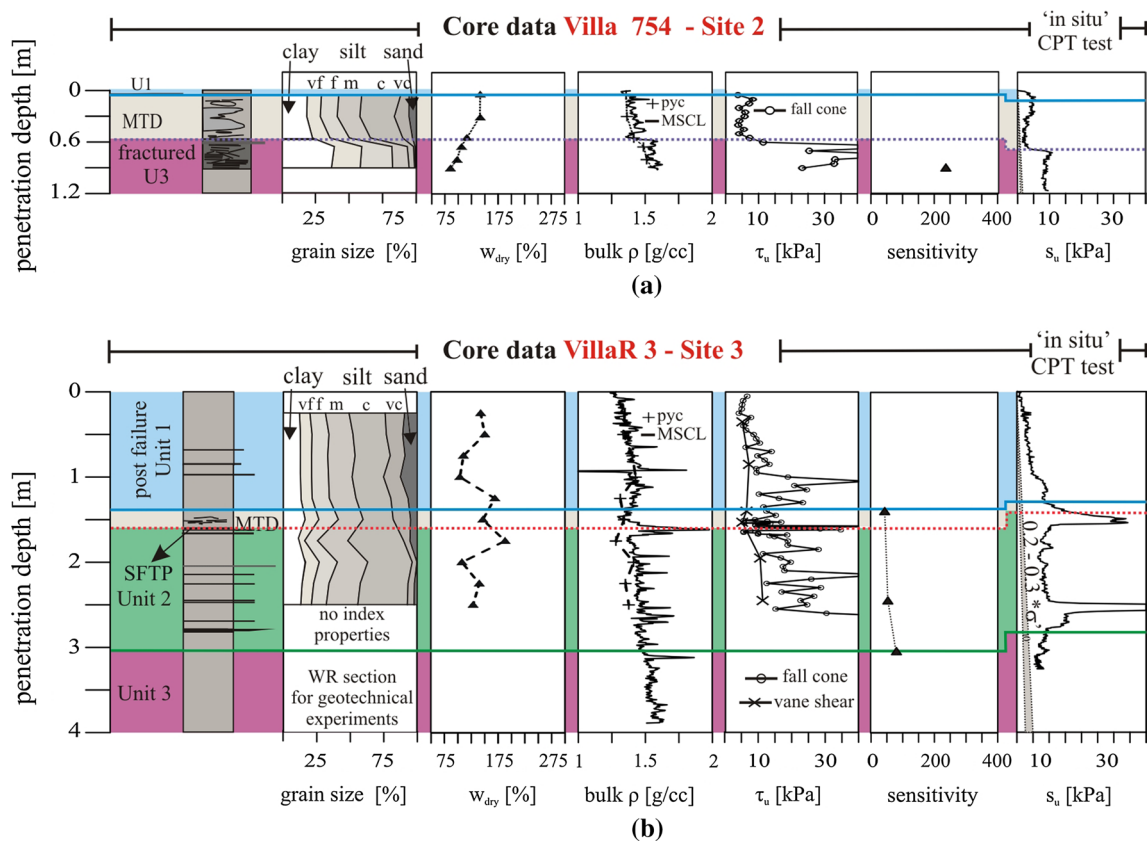
Reference coring site 1: undisturbed plateau

Figure 4 shows the composite plot of all data obtained at the reference site 1.2 including a short segment of reflection seismic data of profile A (Fig. 3a). The sediment core VillaR 1 is ~8 m long. Three distinct units were identified based on abrupt changes in physical and lithological properties measured in cores. These units correspond to specific features in the depositional geometry and correlate with acoustic facies observed in reflection seismic data (U1–U3) (Figs. 3a, b, 4). Tephra layers found in the sequence suggest that it covers the past ~13 kilo years. These tephra deposits include the ~3.8 kilo year Pucón event (Silva Parejas et al. 2010; Heirman 2011) and the ~11 kilo year Neltume pumice (Echegaray et al. 1994). Furthermore, AMS radiocarbon dating was performed at the Ion beam Physics Laboratory of ETH Zürich (Switzerland) on a leaf found in VillaR 1 at a sediment depth of 7.29 m (ETH-52078), very close to the U2–U3 boundary. It provided a 14C age of 10.841 ± 42 years BP which corresponds to a calibrated age (ShCal13) of 12,670–12,755 cal. years BP (2σ). This led to inferred sedimentation rates in the range of 0.4–0.8 mm/year in U1 and U2 sediment at this specific location. Deposition of U3 is believed to have started around 17.5–17.1 kilo years BP, with regional deglaciation (McCulloch et al. 2000). By applying this date to U3, we obtain a sedimentation rate of about 3 mm/yr at site 1.2.

U1 covers the first 0–2.85 mblb and mainly consists of greenish, brownish, finely laminated, diatomaceous ooze (Noorany 1989). Thin (0.1–1.5 cm) tephra layers occur regularly and are considered to be part of the background sediment. U1 is a sandy silt with ~75 % silt-size, diatom frustules. The amount of sand size detrital particles decreases

gradually from ~19 to ~8 % toward the bottom of U1 (Fig. 4). The dry natural water content (w_n %) ranges from 119 to 166 % with a bulk density of ~1.4–1.5 g/cc. Peaks in bulk density coincide with peaks in magnetic susceptibility and correlate with the occurrence of tephra layers. The liquid limit (LL) of U1 (~90 %) was measured at ~1.25 mblb. It is lower than the value of w_n %. The plasticity index (PI) is ~50 %. Sensitivity values are >16, and thus, U1 may technically be termed medium quick clay (Rosenqvist 1953). The influence of diatom frustules on the Atterberg limits and the sensitivity will be discussed in Sect. 8. The "in situ" undrained shear strength (s_u) increases almost linearly from 0 to 15 kPa between 0 and 2.85 mblb which is more than 40 % of the effective overburden stress (σ'_{v0}). The laboratory-derived undrained shear strength (τ_u) shows an equivalent quasi-linear increase in fall cone and vane shear data. However, the peak values exceed 30 kPa, suggesting that U1 is overconsolidated.

Unit 2 (U2) (2.85–7.25 mblb) has a similar lithological composition as U1, but different physical properties. The sand fraction of U2 decreases by 5 %, whereas the silt fraction (mainly coarse silt, i.e., diatom frustules) increases by 5 % with respect to U1. Peaks in the sand fraction within the grain size data are related to tephra layers. The main sediment constituent is uniformly finely laminated diatomaceous ooze, with fewer detrital sand particles than in U1 (see SEM images in Fig. 4). Clay content and bulk density slightly increase with depth and reach values of ~20 % and 1.5 g/cc, respectively. The first meter of U2 has a w_n % of ~275 %. Values within the lower portion range from ~90 to ~160 %. At 3.95 and 6.7 mblb, the LL is ~75 and 110 % and therefore smaller than the w_n %. At these depths, PI has a value of 45 % and 22 %, respectively. Sensitivity shows an increasing trend with depth (137–266). U2 may thus technically be termed extra-quick clay (Rosenqvist 1953). The "in situ" undrained shear strength shows a slightly decreasing trend from ~15 ± 5 to 10 kPa with depth. Peak values of 40 kPa and more are related to the presence of tephra layers. Three distinct tephra layers were identified at ~3.1 mblb (s_u = 45 kPa; Pucon event), at 6.05 mblb (s_u = 40 kPa), and at ~7 mblb (s_u = 92 kPa; Neltume pumice). The tephra layer at 6.05 mblb (i.e., SFPT) is located immediately below the upper failure plane (Figs. 2, 3, 4, 7). In contrast to the CPT data, the vane shear strength of U2 slightly increases with depth starting from ~7.5 kPa at the top and reaching ~10 kPa at the bottom. The state of U2 consolidation decreases with depth and reaches ~0.3–0.4 * σ'_{v0} at the bottom.

Unit 3 (U3) comprises the lowermost portion of core VillaR 1. It consists of proglacial extra-quick clay characterized by an increase in clay size fraction by ~20 %. Sensitivity reaches its maximum with a value of 370. w_n % is <100 % and decreases with depth. LL reaches ~80 %

Fig. 5 Index properties of the sediment cores **a** Villa 754 (site 2) and **b** VillaR 3 (site 3) including (from *left* to *right*): a litholog after visual core description and results of grain size analysis, natural water content (w_n), bulk density (ρ), laboratory-based measurements of und-rained shear strength (τ_u), sensitivity, and "in situ" undrained shear strength (s_u). Shear strength data are clipped at 40 kPa. Horizontal lines separate the different units. *Dashed horizontal red line*: location of the "upper failure plane" right above the SFPT

($<w_n$ %). Bulk density jumps to values >1.5 g/cc. SEM images reveal an open and flocculated, detritic particle arrangement and a significant decrease in the amount of diatom frustules. s_u drops to values <10 kPa, whereas vane shear and fall cone data show higher values (τ_u = 10–20 kPa). The fact that τ_u is much higher than s_u may be related to the penetration process of the CPT. Low total resistance values are measured in quick clay (<1 kN in 15 m depth) (Möller and Bergdahl 1982), despite the fact that the peak shear strength of quick clay measured in laboratory may not be particularly low. It is the extremely low remolded shear strength that gives rise to high sensitivity values (Rosenqvist 1966). Hence, the s_u may be underestimated and explain the discrepancy between laboratory and "in situ" shear strength.

Coring site 2: lower failure plane

The sediment core Villa 754 is a short gravity core of 0.9 m length. It was recovered within the "deep slide scar," and it covers parts of the post-failure sediment drape (U1) and about 0.3 m of intact sediment belonging to U3. The

latter represents an interval of brittle "in situ" deformation. Here, U1 and U3 are separated by a MTD of ~38 cm thickness and are further distinguished by differences in grain size, water content, and bulk density similar to what was observed on the undisturbed plateau. The excavated slope sequence comprises parts of U1, all of U2, and parts of U3, and is marked as "slide mass B" in Fig. 4. Figure 5a shows the composite data plot of the core Villa 754. It is certain that the lower failure plane involved in the slope failure of slide mass B is located within the quick clay of U3. However, it is not clear whether core Villa 754 (Fig. 3b) contains a sample of this failure plane since part of the basal shear surface could have been eroded by the overlying MTD. The deposition of the overlying MTD may have entailed erosion of the basal shear surface.

In the following, we will keep the term "lower failure plane." In seismic reflection data, the failure plane can be seen as the limit between clearly stratified reflectors of U1 and the more chaotic facies, U3. Comparing core Villa 754 with the seismic image of site 1.2 (Fig. 3a), we concluded that the lower failure horizon was not recovered at the reference coring site 1.2.

Fig. 6 a Image of core VillaR 1 (i.e., undisturbed plateau site 1.2) showing the SFPT and overlying sediment. **b** Image of core VillaR 3 (i.e., coring site 3, within the slide scar) showing the SFPT underlying the distinct upper failure plane and the MTD deposit

Coring site 3: upper failure plane

Core VillaR 3 was sampled within the upper stratigraphy of the slide scar (Fig. 2). It is about 4 m long and covers the post-failure sediment drape (~1.35 m of U1), the upper failure plane, approximately 1.25 m of unfailed U2, and ~1 m of U3 sediment. By assuming a sedimentation rate of 0.8 mm/year for the post-failure U1 (see Sect. 7.1.1), we infer a slide age of ~1.6 ka BP. The upper failure plane is distinct and located just above the sandy silt tephra layer, already named SFPT (Fig. 6). A marked increase in bulk density within the layer (Fig. 4) is associated with the impedance contrast that gives rise to the strong reflection in the seismic profiles (Fig. 3a, b). The sediment that was moved during slope failure is marked as "slide mass A" in Fig. 4. Figure 5b shows the composite data plot of CPT and coring site 3. The lower section of the core (i.e., U3) was kept as a whole-round sample for further geotechnical experiments. U1 and U2 are separated by a mass transport deposit (MTD) (see also Fig. 6) of ~25 cm thickness and are further distinguished by differences in grain size similar to those described for core VillaR 1. We are confident to have cored the basal shear plane although some uncertainty remains due to possible erosion during the deposition of the overlying MTD. However, the existence of a distinct failure plane giving rise to a clear seismic reflection with the length of the entire slide scar renders previous erosion unlikely.

The only observed anomaly of the failure horizon within U2 is a peak in sensitivity (Fig. 4). Indeed, the upper failure plane is located immediately above a tephra layer (SFPT) (Figs. 4, 5b, 6). However, there are several other tephra layers within U2 with properties comparable to that of the SFPT (Fig. 4; based on macroscopic observation). Therefore, the location of the upper failure plane can neither be explained solely by its physical properties observed in core VillaR 1 nor can the proximity of the SFPT be the sole reason for the development of the upper failure plane.

CPT plateau transect and pseudo-static factor of safety analysis

"In situ" CPTU deployments were carried out to shed light on the spatial variation in shear strength on the undisturbed plateau and its significance for failure localization. Figure 7a shows the "in situ" undrained shear strength (s_u) with depth along an E–W transect across the unfailed plateau (Fig. 3a, c). Due to local sedimentation rate variations (see Fig. 3a), the CPT reached different stratigraphic levels, although the absolute penetration depth does not vary significantly at the three sites. U3 was only reached at reference coring site 1.2. At site 1.1 and site 1.3, CPT penetration stops within U2, right in the Neltume pumice layer (located at 7 mblb at site 1.2) and ~20 cm above the SFPT, respectively (Fig. 3a). At all three sites, the shear strength increases from 0 to ~15 kPa toward the bottom of U1. U2 shows a decreasing trend of undrained shear strength with depth at all sites; the gradient of which becomes steeper toward sites located closer to the head scarp. Close to the head scarp, the shear strength above the SFPT (~5 kPa) is about two times lower than at the reference site 1.2 (~11.5 kPa). Values as low as 5 kPa are reached only within U3 at the reference site, but these values might not represent the actual peak "in situ" undrained shear strength as mentioned before in Sect. 7.1.1. Furthermore, the shear strength decrease within U2 trends toward values that would be expected in normally consolidated sediment (as indicated by the gray-shaded normal consolidation lines in Fig. 7a, b).
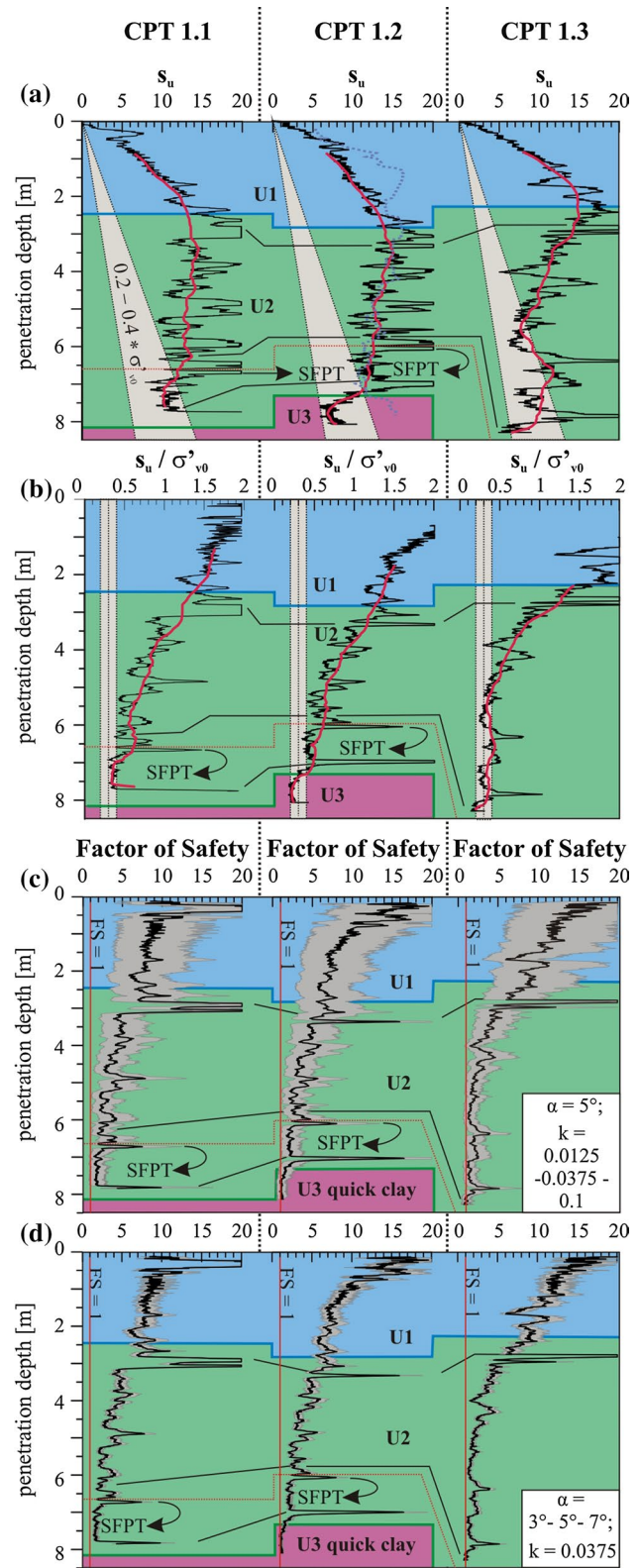
Figure 7b shows the shear strength normalized relative to effective overburden stress. Dashed vertical lines indicate the range of normal consolidation from 0.2 to 0.4 * σ'_{v0}. U1 and the top of U2 are overconsolidated (OC) whereby the OC decreases gradually with depth. At site 1.1 and 1.2, U2 sediment shows values of $s_u/\sigma'_{v0} > 0.3$ except within the sediment segment right below the SFPT at site 1.1.Within U2 at site 1.3, s_u/σ'_{v0} is less than 0.3 below a depth of ~3.9 mblb, and 20 cm above the SFPT, it decreases to values <0.2, suggesting underconsolidated sediment. As the shear strength generally decreases with depth at all sites, we can expect even higher underconsolidation deeper in the strata at site 1.3.

The factor of safety was calculated for different k values (i.e., earthquake intensities) and slope angles at site 1.1–1.3 (Fig. 7c, d) using Eq. 4. It was found that the FS generally decreases with depth independent of the *k* value and/or slope angle which is consistent with the observed decrease in the OC. Peaks in the FS correspond to peaks

—

Fig. 7 a "In situ" undrained shear strength along the transect cutting through the unfailed plateau. *Gray-shaded area* indicates the undrained shear strength of normally consolidated sediments (0.2–0.4 * σ'_{v0}). *Red lines* moving average over 151 data points. *Gray dotted line* (CPT 1.2): moving average over 7 data points of laboratory-derived undrained shear strength (fall cone). For scale purposes, data are clipped at 20 kPa. b Normalized "in situ" undrained shear strength (clipped at values ≤2). *Gray-shaded area* ($s_u/\sigma'_{v0} = 0.2$–0.4). c Estimated factor of safety for a constant slope angle of 5°, varying the seismic coefficient k; *gray-shaded area* $s_u/\sigma'_{v0} = 0.2$–0.4. d Estimated factor of safety with a constant seismic coefficient of 0.0375 and varying slope angle α; *red vertical lines* in Fig. 7c, d indicate the limit between stability (FS > 1) and instability (FS < 1)
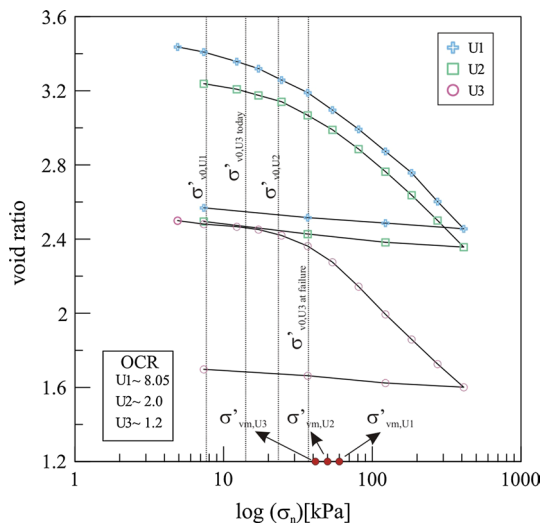

in cone resistance, which are related to relatively high shear strength of tephra layers. At a constant slope angle of 5° and varying *k* values (Fig. 7c), it is seen that the influence of the *k* value variation (width of gray-shaded area) decreases with depth. Figure 7d shows equivalent results for varying slope angles at constant *k* value. Within U2, the FS decreases both with depth and with increasing sedimentation rate from site 1.2 to site 1.3, analogue to the normalized undrained shear strength. The FS values averaged over the entire U2 segments at CPT sites 1.1, 1.2, and 1.3 are 3.8, 3.8, and 2.9, respectively. The analysis shows that an earthquake of MM ≥ VIII (*k* = 0.1) would lead to FS < 1 at all sites at slightly different levels; however, site 1.3 stands out with low FS values regardless of the MM. Large megathrust earthquakes in Chile (M > 8) give intensities of VIII near the rupture plane and can reach VII–VIII at the lake (Moernaut et al. 2014; USGS 2010). Considering a MM of VII, i.e., an event comparable to the 2010 Chile earthquake, FS < 1 would only be reached at site 1.3–20 cm above the SFPT. An earthquake of MM = VI (*k* = 0.0125) leads to FS values > 1 at all sites, however, at site 1.3–20 cm above the SFPT, FS is 1.2, i.e., close to failure. The spatial variance along the plateau transect shows that the FS is (1) lower close to the head scarp and (2) lowest close to the head scarp slightly above the SFPT.

As s_u and FS values surrounding the upper failure plane at site 1.1 and 1.2 are even lower than s_u of the upper failure plane, another mechanism must have taken place in order to reduce the shear strength and create failure at the exact horizon above the SFPT, i.e., the upper failure plane. This observation leads us to the hypothesis that SFPT might have facilitated slope instability. Furthermore, given the uncertainty about the s_u in U3, advanced geotechnical experiments (Sect. 7.4) helped to reveal whether the quick clay or the U2 sediment is more susceptible to failure under static and cyclic loading than the tephra. The approach further allowed an evaluation of how the sediments involved in mass wasting respond to dynamic strength reduction, an aspect which has been ignored in the FS analysis.

One-dimensional compression tests

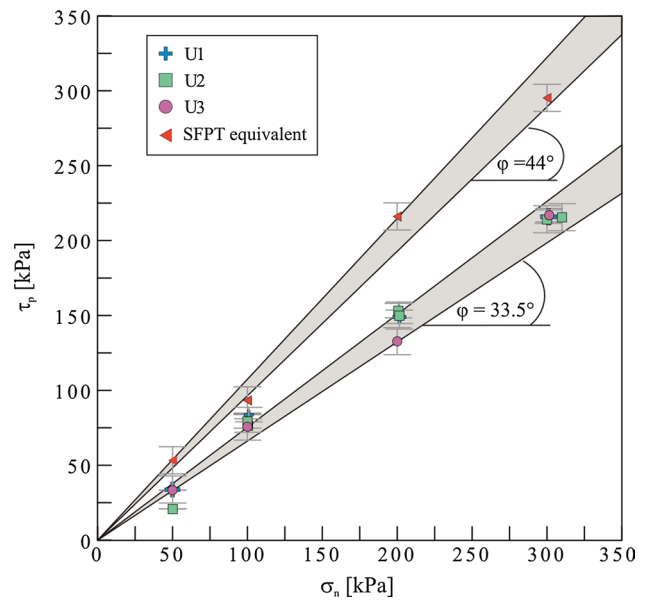Figure 8 presents a plot of the void ratio against the logarithm of vertical stress of U1, U2, and U3 sediment under

Fig. 8 Results from one-dimensional compression tests on samples of U1, U2, and U3. We deduce the maximum past overburden stress ($\sigma'_{v,m}$) after (Schmertmann 1953) (*red dots*). *Vertical dotted lines* indicate the overburden stress ($\sigma'_{v,0}$) at sampling depth. *Two vertical lines* are shown for U3 sample, one representing the vertical overburden stress at present and another representing the vertical overburden stress at the moment of failure (burial depth of 9 mblb, deduced from seismic reflection data)

Fig. 9 Peak shear strength determined in a direct shear apparatus is plotted against effective normal stress. The error in peak shear stress is related to cell friction. Diatomaceous sediments (U1 and U2) have very high drained shear strength values similar to quartz sand, and the SFPT shows even higher values expected in highly angular sands (Bolton 1986)
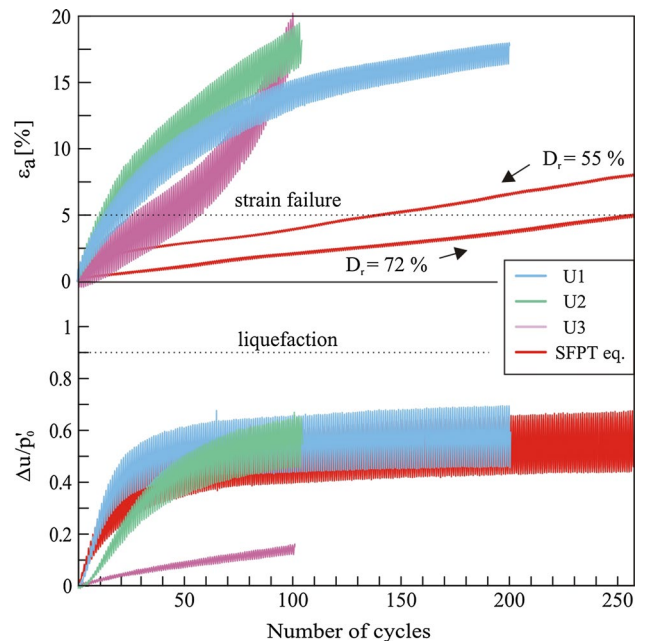
one-dimensional compression. Results show that the initial void ratio decreases markedly from U2 to U3 which can be explained by the relatively hollow structure of diatom frustules. The overconsolidation ratio (OCR $= \sigma'_{v0}/\sigma'_{v0,m}$) decreases remarkably from U1 (OCR $= 8.05$) to U2 (OCR $= 2.0$). U3 has an OCR of 1.2 if a past burial depth of 9 mblb is assumed (Fig. 8) and an OCR of 2.97 if we consider the actual burial depth of 3.69 mblb. Sediments with an OCR of 8.05 and 2 are expected to show normalized undrained shear strengths values of ~1.5 and ~0.5, respectively (Andresen et al. 1979). The values of the normalized undrained shear strength that were derived via the consolidation tests are comparable to the ones calculated from the CPT data (Figs. 5b, 7b). The values of hydraulic conductivity (k_f) determined at a normal stress increase from 81 kPa to 123 kPa for U1, U2, and U3 are 1.1×10^{-7}, 1×10^{-7}, and 6.1×10^{-8} cm/s, respectively. The hydraulic conductivity measured in U3 is one order of magnitude lower than in U1 and U2, which shows values that are typical for clay or silty clay (Fetter 2001).

Advanced geotechnical shear experiments

Drained direct shear tests did not reveal significant differences between the different units (Fig. 9). The internal friction angle of U1, U2, and U3 sediment range from φ ~33.5°

Fig. 10 Cyclic triaxial shear tests on units 1–3 (U1, U2, and U3) samples and the failure plane tephra (SFPT) equivalent. D_r stands for relative density. $D_r = 55$ % is a medium dense sample, $D_r = 72$ % is a dense sample. See Table 1 for details

to 37°. There are no major differences in the drained shear strength of the lower and upper failure plane sediment. For comparative reasons, we also tested the SFPT equivalent for its drained shear strength, which proved to be high with $\varphi \sim 45°$.

In cyclic triaxial tests, an earthquake of MM Intensity of VIII (i.e., PGA = 0.25 g) was simulated. Figure 10 shows the resulting pore pressure ratio (PPR) and axial strain (ε_a) measured in all three units as well as in the material equivalent to SFPT. The test conditions are listed in Table 1. During cyclic loading, the PPR increases rapidly in U1 and U2 samples and in the SFPT equivalent. Within the first 20 loading cycles, PPR reaches 40–50 % of p_0. After 50–70 cycles, the PPR reaches their maximum of ~65–75 %. However, these samples did not reach the liquefaction criteria (PPR = 90 %), which is related to the anisotropic testing conditions (Erguvanil 1980). In contrast to the behavior of U1, U2, and the SFPT equivalent material, the pore pressure build up in U3 quick clay is slow, reaching ~20 % of p_0 after 100 loading cycles. The $\varepsilon_a = 5$ % failure criterion (Garga and McKay 1984) is first reached by the U2 sample, followed by U1 and U3, and finally the SFPT equivalent. Although pore pressure evolution within the U1, U2, and tephra samples is similar, the axial strain evolution differs significantly. After an initial settling phase, ε_a of the tephra samples increases approximately linearly and reaches 5 % ε_a after more than 100 cycles. U1 and U2 sediment build up strain and pore pressure rapidly within the first 0–20 cycles and subsequently reduce the PPR and ε_a increase per cycle. U3 sediment increases its ε_a gradient with increasing number of cycles. Progressive failure and inherent remolding of the sediment seem to favor ε_a accumulation so that 20 % ε_a is first reached by U3 quick clay and then by U2 diatomaceous ooze, which is consistent with the observations made on sensitivity.

Discussion

Based on the geotechnical tests and the analysis of CPT data described above, several key points can be derived.

Data quality

The geotechnical data acquired "in situ" and in the laboratory are considered to be of good quality. Bias induced by dynamic penetration (CPT data) or coring disturbance (laboratory data) is thought to be minor. Several aspects support this assumption: (1) The sediment observed in cores was perfectly horizontally laminated, (2) good correlation of seismic reflection, CPT, and core data indicates minor compaction or sediment distortion due to coring, (3) preconsolidation stress determined from "in situ" CPT data

and laboratory one-dimensional compression tests present equivalent results, and (4) undrained shear strength values determined "in situ" approximately match the ones derived in the laboratory over a wide depth range (Fig. 7a). Any differences between the two are thought to be related to "in situ" excess pore pressure (see Sect. 8.2).

Failure planes and sediment physical properties

Sensitivity

Geotechnical laboratory tests and sediment characterization revealed that sensitivity (i.e., the ratio of peak to remolded shear strength) is the only sediment property in which the upper and lower failure planes clearly differ from the rest of the sediment sequence. Extremely sensitive clay (quick clay) is defined as sediment that has a sensitivity value greater than 30 (Torrance 1983). The term "clay" here refers to grain size and not to mineralogy. Clay-size particles with low activity (quartz, feldspar, amphibole, hydrous mica, and chlorite) may arrange in a high void ratio, flocculated structure that resists consolidation and therefore remains at near-constant water content during burial. This structure is typical for post-glacial, fine-grained sediments (Torrance 1983). U3 sediment is a paradigm of quick clay (sensitivity >200, Figs. 4, 5a).

U2 sediment has a natural water content larger than its liquid limit ($w_n\% >$ LL) (Fig. 4) and, thus, may technically be termed "quick clay," but as it contains ~45–50 % coarse silt and sand (Fig. 4), the flocculation of particles is unlikely. U2 has special physical properties due to the high amount of diatom frustules (SEM pictures Fig. 4). Diatoms are hollow silicious microfossil shells bearing internal water, which explains high natural water contents, low bulk densities (Day 1995) (Fig. 4), and high void ratios (Fig. 8). During remolding, the shell internal water may become interstitial water and leads to liquefaction of the material. The LL is reached once most of the "excess" shell internal water is expelled. Hence, LL < w_n % makes the sediment highly sensitive and similar to classical quick clay once remolded.

Using sensitivity as single indicator for the sediment's susceptibility to failure is questionable because a high sensitivity value mainly suggests that remolded shear strength is extremely low. In order to produce failure and subsequently remold the sediment, peak shear strength must be exceeded in the first place. Sensitivity can be a leading factor in a progressive failure process under quasi-static conditions (Urciuoli et al. 2007), but this eventuality was rejected as a potential failure mechanism due to (1) high internal friction angles ($\varphi > 30°$) (Fig. 9) in all slope sediments that make static failure on a 5° slope unlikely, (2) high "in situ" undrained shear strength (s_u) values (Fig. 7a),

and (3) FS ~ 1 only if strong earthquake shaking is presumed. "In situ" undrained and cyclic shear strengths are most important parameters in slope stability analysis and need to be taken into account.

In situ undrained shear strength and state of consolidation

The "in situ" undrained shear strength was determined along an E–W transect on the undisturbed plateau (Figs. 3a, c, 7). This transect allows the identification of changes in shear strength in a 2D space. Normalized shear strength (Fig. 7b) and the results of one-dimensional compression tests (Fig. 8) both suggested that the sediment in U1 and the upper portion of U2 is highly overconsolidated. However, it is considered to be an "apparent overconsolidation." Apparent overconsolidation (AOC) typically occurs within the uppermost sediment cover of 0–5 m (Sultan et al. 2000). The AOC is thought to be related to weak interparticle bonds, bioturbation, strengthening by currents and wave action or seismic shaking. At Lake Villarrica, currents and wave action are caused by a strong, westward blowing wind called Puelche (Meruane Naranjo 2005). The AOC commonly decreases with depth (Busch and Keller 1981; Lee and Baraza 1999; Suess et al. 1990) which might be the reason for the observed decrease in s_u/σ'_{v0} within U1 and the upper portion of U2. From Fig. 7, we can conclude that potential shear failure is restricted to the zone below the AOC (AOC 0 to ~6 mblb at site 1.1 and 1.2 and 0 to ~4 mblb at site 1.3). With continuous sedimentation, the AOC moves upward. Thus, a layer or stratigraphic boundary with the potential to turn into a failure plane must first be buried to a certain depth before it becomes critical for landslide initiation.

The decrease in s_u with depth (Fig. 7a) is thought to be related to the existence of overpressure. Evidence for remaining overpressure is particularly given at site 1.3, close to the head scarp, where the sediment is underconsolidated ($s_u/\sigma'_{v0} < 0.2$). Sedimentation rates of 0.4–0.8 mm/year are considered too low to generate overpressure at shallow depth (Dugan and Germaine 2008) and inherent shear strength reduction with depth. Nevertheless, hydraulic conductivity of U1 and U2 is extremely low, particularly regarding the high amount of diatoms. Therefore, we suggest that the observed high AOC and low hydraulic conductivity in U1 and U2 are linked and that there is a fluid source at greater depth. Further we hypothesize a fluid source at depth that may evacuate through focused fluid escape conduits to create overpressure at shallow depths (Dugan and Germaine 2008). It seems likely that the overpressure potentially created below U3 gets locally constrained and follows existing fluid paths along fractures that are present as brittle failures in U3 (gravity core Villa 754).

In any case, low s_u values shortly above the SFPT at site 1.3 may be directly related to excess pore pressure.
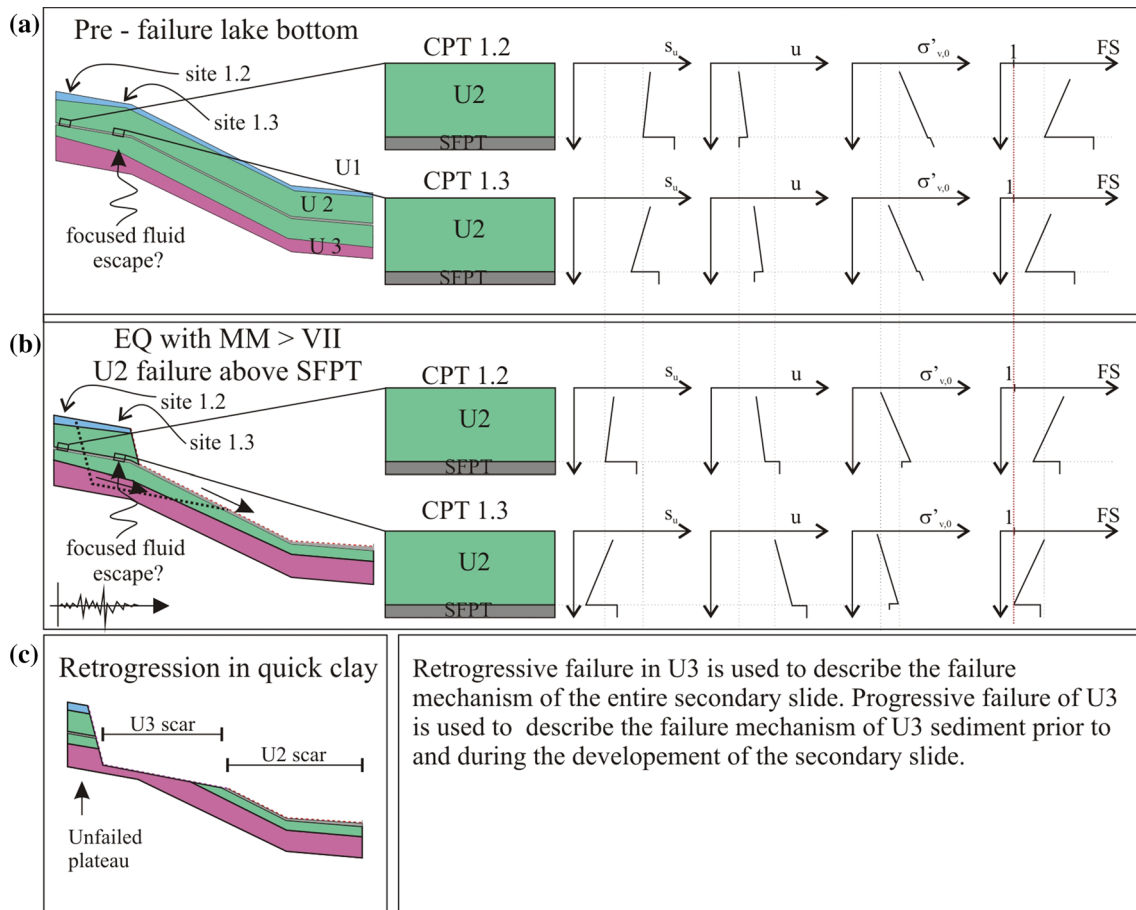
However, this factor alone does not fully explain the location of the upper failure plane as even lower s_u values can be expected at greater depths as inferred from the continuous decrease in s_u below the SFPT at sites 1.1 and 1.2. Hence, the excess pore pressure build up within the SFPT generated during earthquake shaking (Fig. 10) must have turned the boundary to U2 into the weakest horizon in the sequence.

The role of ash

Tephra layers are presumed to have high liquefaction susceptibility and may represent preferred failure planes of submarine slides in active geological settings (Sassa et al. 2012; Harders et al. 2010). However, not every tephra layer is a failure plane and not every failure plane is close to a tephra layer in such settings. Our data from Lake Villarrica clearly indicate that neither the tephra layer at 3.1 mblb nor the pumice layer at 7 mblb ever acted as a failure plane in our study area. Since the pumice layer at 7 m is older than the SFPT, it experienced significantly larger amount of high magnitude earthquakes than the SFPT and must have had the opportunity to liquefy many more times. The discrepancy can be explained with the anisotropic, undrained, cyclic triaxial data that show three main results: (1) U2 sediment builds up significant axial strain and pore pressure, (2) the failure plane SFPT equivalent only slowly accumulates axial strain, but pore pressure increases very fast in comparison with U2 and U3 sediment, and (3) the U3 quick clay neither quickly accumulates axial strain nor does the pore pressure rise significantly during initial cyclic loading (Fig. 10). These data give evidence for the fact that flow liquefaction did not occur within the SFPT. Instead, slope failure initiation immediately above the SFPT (Fig. 6) might have resulted from both a pore pressure build up and contrast between the highly permeable SFPT and the weak, low-permeable U2 sediment right above it. While excess pore pressure might have been too low to overcome the undrained shear strength within the SFPT, there could still have been enough pore pressure to cause a reduction in sediment strength along the interface of U2 and the SFPT. Once the peak undrained shear strength was exceeded, the high sensitivity and lateral continuity of the horizon led to the development of a slope-parallel shear plane promoting translational sliding over large distances (Fig. 11). This failure mechanism was facilitated by the lateral continuity of the SFPT over large distances.

The role of quick clay

Quick clay slides are known to be predominantly retrogressive in nature. In Lake Villarrica, there are multiple pieces of evidence that the lower failure plane (U3 quick clay) was

Fig. 11 *Left* **a, b** and **c** Simplified model for landslide process. *Right* illustration of undrained shear strength (s_u), sediment excess pore pressure (u), effective overburden (σ'_{v0}), and factor of safety (FS) at the interface of the SFPT and U2 at site 1.2 and 1.3 (**a**) prior to earthquake shaking and (**b**) after earthquake shaking

activated after the failure of the upper failure plane (U2 horizon) had occurred: (1) From a morphological point of view, the "bottle-neck-shaped" outlet (Figs. 2, 3) points toward retrogression (Ter-Stepanian 2000) and (2) Neither in static nor in cyclic loading experiments (Figs. 9, 10) do the quick clays show low shear strength values. Moreover, progressive failure in cyclic loading experiments (Fig. 10) promotes retrogression and even the liquefaction needed to produce a "bottle-neck-shape" outlet.

Retrogression may explain the observed scarp geometries and the existence of two failure planes (Fig. 11): After the destabilization of the upper failure plane, the subsequent mass movement removed the material serving as backstop for the quick clay unit (U3) and local strain started to accumulated (Fig. 10). With the gradual increase in strain (brittle failure) and shear strength reduction in U3 sediment, progressive slope failure was initiated. Mass movement led to the complete remolding of the entire sediment sequence and ended in the transportation of material along the "bottle-neck-shaped" channel. The time that may

have elapsed between U2 and U3 failure could not be determined with certainty. Both might have failed as two separate events, but closely spaced in time as can be expected when triggered, for example, by a major earthquake followed by an aftershock.

Conclusion

This study clearly shows that a coupled "in situ" and laboratory geotechnical approach is needed to reveal and fully understand the complex nature of geohazards. Results suggest that static, gravitational slope failure under drained conditions could not have been possible because the high angles of internal friction (Fig. 7) render failure on a 5° slope unlikely. Instead, an additional external trigger is required, which we have approximated in this study as an earthquake of Modified Mercalli Intensity (MM) of ~VII or higher. Because of possible site effects such as wave attenuation or amplification due to soft mud, our results

should be regarded as first-order approximation. Sediment failure occurred within U2 diatomaceous ooze just above a tephra layer. Pore pressure increase and inherent reduction in effective stresses at the contact surface of the tephra layer and the weak, underconsolidated diatomaceous background sediment triggered a first failure phase. Subsequent quick clay failure occurred in retrogression as a result of the first failure phase that facilitated ramp-out after backstop removal (Fig. 11). The assumption that the subaqueous slides in Lake Villarrica were earthquake-triggered has so far been based on interpretation of seismic reflection data (Moernaut et al. 2009). This is now also supported by geotechnical data.

The results from the geotechnical experiments conducted in this study allow for a number of additional conclusions with global significance for larger submarine slope failures:

- Complete liquefaction of deeply buried tephra is unlikely due to anisotropic stress conditions and cyclic strengthening effects in which repeated earthquake shaking progressively dewaters and thus strengthens the sediment. However, this needs further proof.
- Sediment that is rich in diatoms has fundamentally different physical properties compared to organic or inorganic soils, and conventional geotechnical methods might not be sufficient for a complete characterization. Further examination is necessary for landslide initiation studies as diatomaceous sediment is frequently present in combination with volcanic ash along active margins (Hamme et al. 2010). Furthermore, it has a similar potential to build up pore pressure as silts or sands. Therefore, we agree with Locat and Tanaka (2001) who proposed the introduction of a new class of soil for fossiliferous soils due to their unique behavior.

References

Andresen A, Berre T, Kleven A, Lunne T (1979) Procedures used to obtain soil parameters for foundation engineering in the North Sea. Marine Georesources Geotechnol 3(3):201–266

Angermann D, Klotz J, Reigber C (1999) Space-geodetic estimation of the Nazca–South America Euler vector. Earth Planet Sci Letters 171(3):329–334. doi:10.1016/S0012-821X(99)00173-9

ASTM Standard (2000) Standard test methods for liquid limit, plastic limit, and plasticity index of soils. ASTM International, West Conshohocken, PA

Bertrand S (2005) Sédimentation lacustre postérieure au dernier maximum glaciaire dans les lacs Icalma et Puyehue (Chili meridional): réconstitution de la variabilité climatique et des évènements sismo-tectoniques. Université de Liège, Liège

Blum P (1997) Physical Properties Handbook: A guide to the shopboard measurement of physical properties of dee-sea cores. ODP Technical Notes 26

Blumberg S, Lamy F, Arz HW, Echtler HP, Wiedicke M, Haug GH, Oncken O (2008) Turbiditic trench deposits at the South-Chilean active margin: a Pleistocene-Holocene record of climate and tectonics. Earth Planet Sci Letters 268(3–4):526–539

Bolton MD (1986) The strength and dilatancy of sand. Geotechnique 36(1):65–78

British-Standard-Institute (1977) Methods of testing soil for civil engineering purposes, BS 1377. BSI, London, vol BS1377. BSI, London

Busch WH, Keller GH (1981) The physical properties of Peru–Chile continental margin sediments; the influence of coastal upwelling on sediment properties. J Sediment Res 51(3):705–719

Chaney RC, Richardson GN (1988) Measurement of residual/remolded vane shear strength of marine sediments. Vane shear strength testing in soils. In Richards AF (ed), Field and laboratory study, ASTM STP 1014. ASTM, Philadelphia

Chapron E, Ariztegui D, Mulsow S, Villarosa G, Pino M, Outes V, Juvignié E, Crivelli E (2006) Impact of the 1960 major subduction earthquake in Northern Patagonia (Chile, Argentina). Quat Int 158(1):58–71. doi:10.1016/j.quaint.2006.05.017

Cisternas M, Atwater BF, Torrejon F, Sawai Y, Machuca G, Lagos M, Eipert A, Youlton C, Salgado I, Kamataki T, Shishikura M, Rajendran CP, Malik JK, Rizal Y, Husni M (2005) Predecessors of the giant 1960 Chile earthquake. Nature 437(7057):404–407

Day RW (1995) Engineering properties of diatomaceous fill. J Geotech Eng 121(12):908–910

Dayal U, Allen JH (1975) The effect of penetration rate on the strength of remolded clay and sand samples. Can Geotech J 12(3):336–348. doi:10.1139/t75-038

Deutsches Institut für Normung (1996) Baugrund, Untersuchung von Bodenproben—Bestimmung der Dichte nichtbindiger Böden bei lockerster und dichtester Lagerung. DIN-Norm 1826. Beuth, Berlin

Deutsches Institut für Normung (2002) Baugrund, Untersuchung von Bodenproben—Bestimmung der Scherfestigkeit. DIN-Norm 18137-3. Beuth, Berlin

Deutsches Institut für Normung (2012) Soil—investigation and testing—oedometer consolidation test. DIN 18135:2012-04. Beuth, Berlin

Dugan B, Germaine JT (2008) Near-seafloor overpressure in the deepwater Mississippi Canyon, northern Gulf of Mexico. Geophys Res Lett 35(2):L02304. doi:10.1029/2007gl03227

Duke CM, Leeds DJ (1963) Response of soils, foundations, and earth structures to the Chilean earthquakes of 1960. Bull Seismol Soc Am 53:309–357

Echegaray J, Moreno H, López-Escobar L (1994) El deposito de pómez Pliniana del grupo volcanic Mocho-Choshuenco, Andes del sur (40°S), Chile. Actas 7th Chilean Geological Congress. Concepción

Erguvanil S (1980) Effect of anisotropic consolidation on liquefaction. In: Proceedings of the world conference on earthquake engineering, p 163

Fetter C (2001) Applied hydrogeology, vol 3. Prentice Hall, Upper Saddle River

Galandarzadeh A, Ahmadi A (2012) Effects of anisotropic consolidation and stress reversal on the liquefaction resistance of sands and silty sands. Geotech Eng J SEAGS AGSSEA 43(2):33–39

Garga V, McKay L (1984) Cyclic triaxial strength of mine tailings. J Geotech Eng 110(8):1091–1105. doi:10.1061/(ASCE)0733-9410(1984)110:8(1091

Hamme RC, Webley PW, Crawford WR, Whitney FA, DeGrandpre MD, Emerson SR, Eriksen CC, Giesbrecht KE, Gower JFR, Kavanaugh MT, Peña MA, Sabine CL, Batten SD, Coogan LA, Grundle DS, Lockwood D (2010) Volcanic ash fuels anomalous plankton bloom in subarctic northeast Pacific. Geophys Res Lett 37(19):L19604. doi:10.1029/2010gl044629

Hampton MA, Lee HJ, Locat J (1996) Submarine landslides. Rev Geophys 34(1):33–59

Handin J (1969) On the Coulomb–Mohr failure criterion. J Geophys Res 74(22):5343–5348. doi:10.1029/JB074i022p05343

Hansbo S (1957) A new approach to the determination of the shear strength of clay by the fall-cone test. Proc R Swed Geotech Inst, vol 14. Stockholm

Harders R, Kutterolf S, Hensen C, Moerz T, Brueckmann W (2010) Tephra layers: a controlling factor on submarine translational sliding? Geochem Geophys Geosyst 11(5):Q05S23. doi:10.1029/2009gc002844

Heirman K (2011) 'A wind of change': changes in position and intensity of the southern hemisphere westerlies during oxygen isotope stages 3, 2 and 1. Ghent University, Ghent

Hynes-Griffin ME, Franklin AG (1984) Rationalizing the seismic coefficient method. Miscellaneous Paper GL-84-13, US Army Corps of Engineers, Vicksburg, MS

Ikari MJ, Kopf AJ (2011) Cohesive strength of clay-rich sediment. Geophys Res Lett 38:5. doi:10.1029/2011GL047918

Karlsson R, Viberg L (1967) Ratio of c/p in relation to liquid limit and Plasticity Index, with special reference to Swedish clays. In: Proceedings, conference on shear strength properties of natural soils and rocks, vol 1. Oslo

Kramer SL (1996) Geotechnical earthquake engineering. Prentice Hall, New Jersey

Kreiter S, Moerz T, Strasser M, Lange M, Schunn W, Schlue BF, Otto D, Kopf A (2010) Advanced dynamic soil testing—introducing the New Marum dynamic triaxial testing device. In: Mosher DC, Shipp C, Moscardelli L et al (eds) Submarine mass movements and their consequences. Advances in natural and technological hazard research. Springer, Dordrecht, pp 31–42

Kremer K, Simpson G, Girardclos S (2012) Giant Lake Geneva tsunami in AD 563. Nature Geosci 5(11):756–757. http://www.nature.com/ngeo/journal/v5/n11/abs/ngeo1618.html#supplementary-information

Laugenie C (1982) La région des lacs, Chili méridional. Université de Bordeaux III, France

Lazo Hinrichs RG (2008) Estudio de Los Danos de los Terremotos del 21 y 22 de Mayo de 1960. Universidad de Chile, Facultad de Ciencias Fisicas y Matematicas, Departamento de Ingenieria Civil, Santiago de Chile

Lee H, Baraza J (1999) Geotechnical characteristics and slope stability in the Gulf of Cadiz. Mar Geol 155(1–2):173–190

Leroueil S, Vaunat J, Picarelli L, Locat J, Lee Homa J, Faure R (1996) Geotechnical characterization of slope movements. In: Proceeding of international symposium on landslides, Trondheim, pp 53–74

Locat J, Tanaka H (2001) A new class of soils: fossilifereous soils? Proceedings of the 15th international conference on soil mechanics and geotechnical engineering, vol 3. Istanbul

Loizeau J-L, Arbouille D, Santiago S, Vernet J-P (1994) Evaluation of a wide range laser diffraction grain-size analyser for use with sediments. Sedimentology 41:353–361

Lomnitz C (2004) Major earthquakes of Chile: a historical survey, 1535–1960. Seismol Res Lett 75(3):368–378. doi:10.1785/gssrl.75.3.368

Lunne T, Robertson PK, Powell JJM (1997) Cone penetration testing in geotechnical practice. Spon Press, London

McCulloch R, Bentley MJ, Purves RS, Hulton NR, Sugden DE, Clapperton CM (2000) Climatic inferences from glacial and palaeoecological evidence at the last glacial termination, southern South America. J Q Sci 15(4):409–417

Medvedev SV (1977) Seismic intensity scale MSK-76. Publ Inst Geophys Pol Acad Sc 117:95–102

Meruane Naranjo CB (2005) El Efecto del Viento Puelche sobre la Hidrodinamica y Calidad de Aguas del Lago Villarrica. Santiago de Chile

Moernaut J, De Batist M (2011) Frontal emplacement and mobility of sublacustrine landslides: results from morphometric and seismostratigraphic analysis. Mar Geol 285(1–4):29–45. doi:10.1016/j.margeo.2011.05.001

Moernaut J, De Batist M, Charlet F, Heirman K, Chapron E, Pino M, Brummer R, Urrutia R (2007) Giant earthquakes in South-Central Chile revealed by Holocene mass-wasting events in Lake Puyehue. Sediment Geol 195(3–4):239–256

Moernaut J, De Batist M, Heirman K, Van Daele M, Pino M, Brümmer R, Urrutia R (2009) Fluidization of buried mass-wasting deposits in lake sediments and its relevance for paleoseismology: results from a reflection seismic study of lakes Villarrica and Calafquén (South-Central Chile). Sediment Geol 213:121–135

Moernaut J, Daele MV, Heirman K, Fontijn K, Strasser M, Pino M, Urrutia R, De Batist M (2014) Lacustrine turbidites as a tool for quantitative earthquake reconstruction: new evidence for a variable rupture mode in south central Chile. J Geophys Res Solid Earth 119(3):1607–1633

Mohamad R, Dobry R (1986) Undrained monotonic and cyclic triaxial strength of sand. J Geotech Eng 112(10):941–958. doi:10.1061/(ASCE)0733-9410(1986)112:10(941

Möller B, Bergdahl U (1982) Estimation of the sensitivity of soft clays from static and weight sounding tests. In: Proceedings of the European symposium on penetration testing, pp 291–295

Morgenstern NR, Price VE (1965) Analysis of stability of general slip surfaces. Geotechnique 15(1):79–93

Noorany I (1989) Classification of marine sediments. J Geotech Eng 115(1):23–37. doi:10.1061/(ASCE)0733-9410(1989)115:1(23)

Rosenqvist IT (1953) Considerations on the sensitivity of Norwegian quick-clays. Geotechnique 3(5):195–200. doi:10.1680/geot.1953.3.5.195

Rosenqvist IT (1966) Norwegian research into the properties of quick clay—a review. Eng Geol 1(6):445–450. doi:10.1016/0013-7952(66)90020-2

Sassa K, He B, Miyagi T, Strasser M, Konagai K, Ostric M, Setiawan H, Takara K, Nagai O, Yamashiki Y, Tutumi S (2012) A hypothesis of the Senoumi submarine megaslide in Suruga Bay in Japan—based on the undrained dynamic-loading ring shear tests and computer simulation. Landslides 9(4):439-455. doi:10.1007/s10346-012-0356-2

Schmertmann JH (1953) The undisturbed consolidation behavior of clay. Proc ASCE 79:1–26

Seed HB, Idriss IM (1971) Simplified procedure for evaluation soil liquefaction potential. Soil Mech Found Eng SM 9:1249–1273

Silva Parejas C, Druitt TH, Robin C, Moreno H, Naranjo JA (2010) The Holocene Pucón eruption of Volcán Villarrica, Chile: deposit architecture and eruption chronology. Bull Volcanol 72(6):677–692. doi:10.1007/s00445-010-0348-9

Skempton AW (1954) The pore pressure coefficients A and B. Geotech 4(4):143–147

Stegmann S, Villinger H, Kopf A (2006) Design of a modular, marine free-fall cone penetrometer. Sea Technol 47(2):27

Stegmann S, Strasser M, Kopf A, Anselmetti FS (2007) Geotechnical in situ characterisation of subaquatic slopes: the role of pore

pressure transients versus frictional strength in landslide initiation. Geophys Res Lett 34:L07607

Strasser M, Stegmann S, Bussmann F, Anselmetti FS, Rick B, Kopf A (2007) Quantifying subaqueous slope stability during seismic shaking: Lake Luceren as model for ocean margins. Mar Geol 240:77–97

Suess E, von Huene R, Lee HJ, Kayen RE, McArthur WG (1990) Consolidation, triaxial shear-strength, and Index-Property characteristics of organic-rich sediment from the Peru continental margin: results from Leg 112. In: Proceedings of the ocean drilling program, scientific results, vol 112

Sultan N, Cochonat P, Dennielou B, Bourillet JF, Savoye B, Colliat JL (2000) Surconsolidatoin apparente et pression osmotique dans un sédiment marin (Appearant overconsolidation and osmotic pressures in marine sediments). CRAcadSciParis, Sience de la Terre et des planètes 331:379–386

Sultan N, Cochonat P, Canals M, Cattaneo A, Dennielou B, Haflidason H, Laberg JS, Long D, Mienert J, Trincardi J (2004) Triggering mechanisms of slope instability processes and sediment failures on continental margins: a geotechnical approach. Mar Geol 213(1–4):291–321

Syvitski JPM, Asprey KW, Clattenburg DA (1991) Principles, design and calibration of settling tubes. Principles, methods and application of particle size analysis. Cambridge University Press, New York

Tanaka M, Watabe Y, Tomita R, Kamei T (2012) Effects of diatom microfossils content on physical properties of clays. In: Proceedings of the twenty-second international offshore and polar engineering conference. ISOPE, Rhodes, Greece, 17–22 June 2012

Ter-Stepanian G (2000) Quick clay landslides: their enigmatic features and mechanism. Bull Eng Geol Environ 59(1):47–57. doi:10.1007/s100640000052

Torrance JK (1983) Towards a general model of quick clay development. Sedimentology 30(4):547–555

Urciuoli G, Picarelli L, Leroueil S (2007) Local soil failure before general slope failure. Geotech Geol Eng 25(1):103–122. doi:10.1007/s10706-006-0009-0

USGS (2010) Pager—M 8.8—Offshore Maule, Chile

Volpi V, Camerlenghi A, Hillenbrand CD, Rebesco M, Ivaldi R (2003) Effects of biogenic silica on sediment compaction and slope stability on the Pacific margin of the Antarctic Peninsula. Basin Res 15(3):339–363. doi:10.1046/j.1365-2117.2003.00210.x

Witter JB, Kress VC, Delmelle P, Stix J (2004) Volatile degassing, petrology, and magma dynamics of the Villarrica Lava Lake, Southern Chile. J Volcanol Geotherm Res 134(4):303–337. doi:10.1016/j.jvolgeores.2004.03.002

Youd TL, Idriss IM, Andrus RD, Arango I, Castro G, Christian JT, Dobry R, Liam Finn WD, Harder LF Jr., Hynes ME, Ishihara K, Koester JP, Liao SSC, Marcuson WF III, Martin GR, Mitchell JK, Moriwaki Y, Power MS, Robertson PK, Seed RB II KHS (2001) Liquefaction resistance of soils: summary report from the 1996 NCEER and 1998 NCEER/NSF workshops on evaluation of liquefaction resistance of soils. J Geotech Geoenviron Eng 127(10):817–833